HHS Public Access

Author manuscript

ACS Nano. Author manuscript; available in PMC 2018 April 12.

Published in final edited form as:

ACS Nano. 2016 June 28; 10(6): 5687–5695. doi:10.1021/acsnano.6b02435.

Controlled Sculpture of Black Phosphorus Nanoribbons

Paul Masih Das[†,#], **Gopinath Danda**[†,‡,#], **Andrew Cupo**[§,#], **William M. Parkin**[†], **Liangbo Liang**[‖], **Neerav Kharche**[§], **Xi Ling**[⊥], **Shengxi Huang**[⊥], **Mildred S. Dresselhaus**[⊥], **Vincent Meunier**[*,§], and **Marija Drndic**[*,†]

[†]Department of Physics and Astronomy, University of Pennsylvania, Philadelphia, Pennsylvania 19104, United States

[‡]Department of Electrical and Systems Engineering, University of Pennsylvania, Philadelphia, Pennsylvania 19104, United States

[§]Department of Physics, Applied Physics, and Astronomy, Rensselaer Polytechnic Institute, Troy, New York 12180, United States

[‖]Center for Nanophase Materials Sciences, Oak Ridge National Laboratory, Oak Ridge, Tennessee 37831, United States

[⊥]Department of Electrical Engineering and Computer Science, Massachusetts Institute of Technology, Cambridge, Massachusetts 02139, United States

Abstract

Black phosphorus (BP) is a highly anisotropic allotrope of phosphorus with great promise for fast functional electronics and optoelectronics. We demonstrate the controlled structural modification of few-layer BP along arbitrary crystal directions with sub-nanometer precision for the formation of few-nanometer-wide armchair and zigzag BP nanoribbons. Nanoribbons are fabricated, along with nanopores and nanogaps, using a combination of mechanical–liquid exfoliation and *in situ* transmission electron microscopy (TEM) and scanning TEM nanosculpting. We predict that the few-nanometer-wide BP nanoribbons realized experimentally possess clear one-dimensional quantum confinement, even when the systems are made up of a few layers. The demonstration of

[*]**Corresponding Authors:** meuniv@rpi.edu. drndic@physics.upenn.edu.

[#]**Author Contributions**

P.M.D., G.D., and A.C. contributed equally to this work. V.M. and M.D. designed the research plan. P.M.D., X.L., and S.H. assisted in sample preparation. P.M.D. performed AFM measurements. P.M.D., G.D., and W.P. performed TEM, STEM, and SAED measurements and analysis. A.C., N.K., L.L., and V.M. performed all theoretical calculations.

Supporting Information

The Supporting Information is available free of charge on the ACS Publications website at DOI: 10.1021/acsnano.6b02435. Additional time evolutions of elliptical nanopore expansion under electron irradiation, thickness/resolution measurements, and HAADF STEM lattice images; STEM simulations along with the initial and final edge geometries for single atom removal; band structures for ZZ-2 nanoribbons and phosphorene, partial charge densities for the determination of edge bands, and width-dependent thermodynamic stabilities for the monolayer and bulk BP nanoribbons (PDF)

Animation for armchair edge (AVI)

Animation for ZZ-1 edge (AVI)

Animation for ZZRC-i edge (AVI)

Animation for ZZRC-o edge (AVI)

Notes

The authors declare no competing financial interest.

this procedure is key for the development of BP-based electronics, optoelectronics, thermoelectrics, and other applications in reduced dimensions.

Graphical abstract

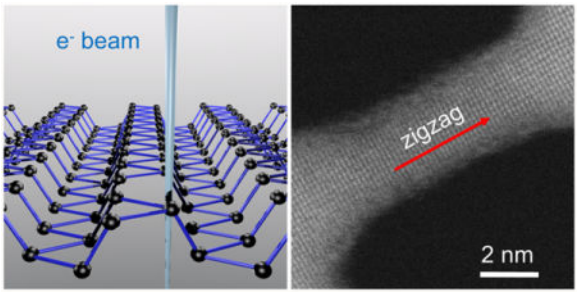

Keywords

few-layer black phosphorus; phosphorene; nanoribbon; nanopore; armchair; zigzag

Few-layer black phosphorus (BP) is an attractive two-dimensional (2D) nanomaterial due to the compromise it offers between high carrier mobility and semiconducting properties found in other layered materials such as graphene and transition metal dichalcogenides (TMDs) like MoS_2.[1–3] BP is a monoelemental realization of phosphorus with a structure characterized by stacked phosphorene monolayers held together by weak forces. The anisotropy in BP results from the existence of two major asymmetric directions with armchair and zigzag arrangements. The armchair (or “light”) direction features a high mobility of around 1000 $cm^2\ V^{-1}\ s^{-1}$, while the zigzag (or “heavy”) direction has a much lower mobility of 600 $cm^2\ V^{-1}\ s^{-1}$.[2] In the current state-of-the-art methods, bulk BP can be exfoliated down to few-layer BP or even monolayer phosphorene *via* mechanical- or liquid-based methods.[4,5] In comparison to other few-atom-thick materials, few-layer BP devices exhibit in-plane anisotropic transport and a thickness-dependent direct band gap (0.3–1.5 eV).[1,6–10] These properties would make few-layer BP a candidate for high-performance optoelectronic applications, once in-air stability issues are resolved, for example, using encapsulation techniques to protect the active phosphorene layer.[11,12]

Confining 2D materials into nanoribbons would constitute a basis for developing 1D nanoelectronics.[13,14] Recent density functional theory (DFT) studies indicate that the transport properties of few-layer BP nanoribbons (BPNRs), such as band gap magnitude and charge carrier effective mass, are sensitive to both ribbon width and crystallographic orientation due to BP’s strongly anisotropic in-plane and interplanar properties.[15,16] Starting from 2D parent structures, top-down approaches have been developed to fabricate 1D nanostructures with either electron-beam nanosculpting[17,18] or optical- or electron-based lithography.[19] However, lithographic techniques for 2D materials usually do not allow the single- or few-atom control available in nanosculpting. For example, few-nanometer-wide nanoribbons and nanopores are readily formed in 2D membranes such as graphene[20] and TMDs such as MoS_2[21] through the focused electron beam of a transmission electron microscope (TEM).

So far, no study has been reported for the fabrication of few-nanometer-wide BPNRs in the few-layer regime. Bottom-up, organic chemistry approaches have been pursued for graphene nanoribbons (GNRs). However, an atom-by-atom approach is unlikely to be developed soon for phosphorene due to its more complex chemistry, which makes it vulnerable to environmental degradation. To date, the narrowest BPNRs were reported by Lee *et al.*, who demonstrated anisotropic thermal conductivities for ribbons down to thicknesses of 50 nm and widths in the mesoscopic range of 500 nm.[22] Understanding the large number of phenomena resulting from 1D confinement in phosphorene requires the ability to fabricate nanostructures with atomic control at size scales small enough to delve into the regime of quantum confinement.[15,23]

Here, we report a top-down method that enables the fabrication of nanopores, nanoribbons, nanogaps, and nanoconstrictions in suspended few-layer BP flakes produced by a combined mechanical–liquid exfoliation procedure. Using a TEM, we first drill nanopores in suspended few-layer BP flakes and show orientation-dependent anisotropic pore expansion under uniform electron irradiation. Starting from nanopores, we fabricate few-nanometer-wide armchair and zigzag BPNRs with sub-nanometer-precise scanning TEM (STEM) nanosculpting. We also complement our results with DFT-based transition state modeling of phosphorene edges and predictions of the electronic properties of 1D BPNRs governed by strong confinement effects.

RESULTS AND DISCUSSION

BP flakes were mechanically exfoliated from bulk BP crystals onto a SiO_2 substrate using blue Nitto tape. The flakes were further exfoliated by sonicating this SiO_2 substrate in dimethylformamide (DMF) for 60 min.[5,24] The BP–DMF dispersions contain few-layer (<20 nm) flakes and are suitable for deposition onto TEM-compatible membranes, which cannot withstand harsh mechanical exfoliation techniques. After sonication, BP–DMF dispersions were drop-cast onto holey carbon grids or holey silicon nitride (SiN_x) membranes, dried in N_2, and annealed at 250 °C in Ar/H_2. Because of the detrimental effects on few-layer BP hole mobility, on/off ratio, and surface roughness from water and light-induced oxidation,[25] all samples were stored in the dark in vacuum (~10 mTorr).

Figure 1a–d shows the deposition of few-layer BP flakes and their structural characterization. Suspended few-layer BP flakes were identified using optical microscopy (Figure 1a). Atomic force microscopy (AFM) scans of suspended flakes on holey SiN_x membranes indicated sample thicknesses from 11 to 20 nm, including the 13 nm sample in Figure 1b. Using high-angle annular dark-field (HAADF) STEM imaging, which produces mass-contrast images, flakes suspended on holey carbon TEM grids were found to have thicknesses in agreement with AFM results (Figure S1) and consistent with previous studies.[26,27] In addition to AFM and optical evidence, we confirmed flake suspension with TEM (Figure 1b inset).

In few-layer BP, layers are stacked in an AB fashion (similar to bulk), in which adjacent layers are shifted by a half-lattice constant in the zigzag direction.[4,28] Figure 1c includes a STEM simulation (top) and a schematic illustration (bottom) of this arrangement in bilayer

BP (see also section S2). Note that, as reported before, the STEM measurements report an image corresponding to projected positions of atoms a few layers deep.[5] Due to BP's AB-stacked configuration, we observe a structure with half-lattice constants a_1' (1.67 Å) and a_2' (2.24 Å) compared to the BP basal plane lattice parameters a_1 (3.34 Å) and a_2 (4.47 Å) along the zigzag and armchair directions, respectively (Figures 1d and S3).[9,28]

High-resolution TEM (HRTEM) images are formed by irradiating a region of interest with an electron beam and monitoring transmitted electrons. The electron beam can also be focused into a small probe and used to drill nanopores, as reported in other materials, such as graphene,[20] MoS_2,[21] and SiN_x.[29] Here, we show that nanopores can be drilled in suspended few-layer BP flakes such as the sample shown in Figure 1e. The selected area electron diffraction (SAED) pattern shown in the inset indicates the orthogonal orientation of the zigzag (200) and armchair (020) axes. Nanopores such as the 10 nm diameter one in Figure 1f were drilled by focusing a TEM beam (probe size ~1.0 nm, probe current = 8.0 nA) for ~1–2 s. Using the orientation of the SAED pattern, which agrees with orientations seen in high-resolution lattice images, L_{200} and L_{020} correspond to nanopore dimensions along the zigzag and armchair directions, respectively. After initial drilling, the ratio of L_{200}/L_{020} was 1.0 as expected for an approximately circular pore. Under an additional 15 min of uniform electron-beam irradiation (current density = 6.1×10^{-2} pA/nm^2) in HRTEM imaging mode, L_{200}/L_{020} is found to increase to a value of 1.4, showing preferential expansion in the zigzag direction (Figure 1f–i), leading to the evolution of the initially circular structure into an elliptical pore (see also Figure S4.1). This is similar to the results of Fortin-Deschênes *et al.*, who reported sublimation-induced, eye-shaped crack propagation along the (100) direction at temperatures between 400 and 500 °C.[30,31] Moving beyond pore formation, the creation of nanoconstrictions and nanogaps in TEM was also observed by first drilling two adjacent pores and then simultaneously exposing them to broad electron-beam irradiation in order to narrow the region between them. The time evolution for an individual nanoconstriction is provided in Figure S4.2.

To explain the anisotropic opening of nanopores under uniform electron-beam irradiation, we calculated the energy barriers for removing single atoms from several known phosphorene edges. We employed first-principles calculations within DFT and energy barrier evaluation using the nudged elastic band (NEB) method (see Methods). Single unit cells of the five edges used and the corresponding edge energies of the supercells used are given in Figure 2a. Initial and final geometries for removing single atoms from various edges are given in Figure S5, and animations for four specific cases are included in the Supporting Information. We considered three zigzag edges (ZZ-1, ZZRC-i, and ZZRC-o) and one armchair edge. The ZZRC-i and ZZRC-o edges are stable reconstructions of the ZZ-2 edge. The resulting energy landscapes shown in Figure 2b indicate that the overall energy barrier is the absolute value of the energy change itself. For armchair, ZZ-1, ZZRC-i, and ZZRC-o, the corresponding energy barriers are 5.13, 5.57, 5.65, and 6.23 eV. Therefore, among these structures, the ZZRC-o edge is the most resistant to the removal of a single atom. Note that for the ZZRC-i case the energy initially decreases because geometries resembling the more stable ZZRC-o edge are intermediate states. For the armchair case, the energy initially increases and then decreases below the zero reference level, which suggests a reconstruction of the edge that is more stable than the standard armchair morphology. Even

when factoring this additional decrease in energy into account, the energy barrier for the ZZRC-o edge is greater than that for the armchair reconstruction. Since the energy barrier for removing an atom from the most stable zigzag edge (ZZRC-o) is greater than that for the armchair edge, we expect the armchair edge to recede faster under symmetric electron-beam irradiation, leaving the zigzag edge relatively longer ($L_{200}/L_{020} > 1$). This accounts for the development of the pores into elliptical shapes, as observed experimentally and illustrated schematically in Figure 2c. Despite the significant decrease in edge energy by passivating the phosphorene edges with hydrogen,[32] we do not consider this here because sample irradiation starts in the middle of the sample and is continuous, thus preventing attachment of hydrogen atoms to the edges. While the DFT calculations presented here using the simplified monolayer phosphorene models qualitatively explain the anisotropic pore expansion observed in experiments, large-scale molecular dynamics simulations involving few layers of BP are required to obtain better connections between theory and the fabrication mechanism.[33]

TEM beams do not offer the sub-nanometer control necessary for the fabrication of BPNRs with a well-defined crystal orientation. Furthermore, current fabrication methods for oriented bulk BPNRs based on electron-beam lithography and reactive ion etching are unsuitable in the sub-50 nm thickness and sub-500 nm width regime.[22] Here, we develop a fabrication procedure for BPNRs in the few-layer thickness, sub-10 nm width regime based on STEM nanosculpting. A focused STEM beam can be rastered over a region of interest to form HAADF images or controllably maneuvered with sub-nanometer precision to make clean cuts through a thin material. STEM-based cutting was already shown to induce fewer defects in graphene[34] and to offer precise nanosculpting of GNRs.[17,35]

We adopted the following strategy to fabricate few-nanometer-wide BPNRs: first, two adjacent nanopores were nanosculpted in a 17 nm thick BP flake (Figure S1) with a focused STEM beam (probe size = 0.15 nm, probe current = 300 pA), and second, the material was sculpted along either the zigzag or armchair direction until the material between them constituted a nanoribbon. Between periods of nanosculpting, the BPNRs were imaged by rastering the electron beam. While the BPNRs experienced thinning during STEM imaging, they remained crystalline, unlike nanostructures exposed to orders of magnitude higher doses in TEM mode (Figure S4.2).[34] In addition to crystalline regions of width w_c, amorphous edges with a roughly constant width $w_r - w_c$ were also seen (Figure 3a,i), where w_r is the total width (see Figure S6.1 for a definition of these quantities). This suggests localized few-layer BP lattice damage and/or small contamination during room-temperature nanosculpting, consistent with results for graphene.[18] Future molecular dynamics simulations could be used to address the issue of layer–layer interactions at ribbon edges and the possible production of phosphorene polymorphs *via* beam-induced heating.[36,37] Nanosculpting works well for cutting through the entire stack (17 nm) of phosphorene layers, indicating that a large amount of material is removed. However, lattice resolution is still achievable, showing the high quality of the nanoribbons.

Figure 3a–h shows the STEM nanosculpting of an 8.0 nm long zigzag few-layer BPNR. From initial widths w_r (w_c) = 7.2 (5.6) nm in Figure 3a, the ribbon was sculpted down to w_r (w_c) = 2.2 (1.0) nm (Figure 3f). The inset in Figure 3b is a fast Fourier transform (FFT) of

the crystalline region outlined in black in Figure 3a and indicates a lattice spacing of 1.65 Å along the nanoribbon axis, which agrees well with the zigzag (200) half-lattice constant a_1' (1.67 Å). The width of the ribbon's amorphous edges ($w_r - w_c$) remained between 0.9 and 1.6 nm (Figure 3a–f). In Figure 3f (w_r (w_c) = 2.2 (1.0) nm), the structure was no longer nanosculpted but rather continuously imaged in STEM mode. After 160 s, the zigzag BPNR was narrowed to a 1.7 nm wide amorphous (w_c = 0 nm) structure and, after an additional 40 s, snapped to form a 3.5 nm wide nanogap (Figure 3g,h).

Figure 3i–p shows the formation of a 6.5 nm long armchair few-layer BPNR using a procedure similar to the one developed for the zigzag system outlined above. From initial widths w_r (w_c) = 6.3 (4.9) nm in Figure 3i, the ribbon was sculpted down to w_r (w_c) = 2.5 (0.5) nm (Figure 3n). Similar to the zigzag case, the width of the ribbon's amorphous edges ($w_r - w_c$) remained fairly constant (between 1.2 and 2.0 nm). As indicated in the inset FFT of Figure 3j, the nanoribbon's axially oriented lattice spacing of 2.28 Å is consistent with the armchair (020) lattice parameter a_2' (2.24 Å). The w_r = 2.1 nm amorphous (w_c = 0 nm) ribbon in Figure 3o was fabricated by allowing the w_r (w_c) = 2.5 (0.5) nm armchair BPNR in Figure 3n to sit in STEM imaging mode for 80 s, similarly suggesting the possibility of narrowing sculpted BPNRs with sub-nanometer precision. A 2.8 nm wide nanogap was formed after an additional 120 s of exposure (Figure 3p).

To determine how narrowing induces quantum confinement in the range of widths achieved here, we calculated DFT-based band structures for single- and multilayer armchair and zigzag-edged structures. For the zigzag case, the ZZ-1 and ZZ-2 edge morphologies were used because the crystalline parts of the ribbons are surrounded by amorphous material, which in a first approximation would constrain the edges to those formed by directly cutting the sheet or bulk. Details of the calculations can be found in Methods, and band structures for phosphorene along the same high symmetry directions are reproduced in Figure S8. Only the four smallest nonzero crystalline widths obtained in the experiment for each edge are shown because the overall structure of the bands changes negligibly for larger widths (Figures 4 and S7). We show that in both 2D (*i.e.*, single-layer) and bulk material, the electronic band structure displays the 1D confinement effects, as indicated by the presence of edge bands, which we determined by calculating and plotting the partial charge density of bands near the Fermi level (Figure S9). This finding results from the weak coupling between the individual phosphorene layers. The edge energies (2D) and surface energies (bulk) are correlated with the widths in Figure S10. Further modeling of the nanosculpting effect would require a systematic study of electron-beam-induced disorder in BP[38] in addition to thermally induced defects.[39]

In addition to nanosculpting as a method of narrowing BPNRs into the quantum confinement regime, ribbons were also found to be thinned during STEM imaging, as evidenced by the evolution of the STEM intensity cross sections (Figure 3a,i). Average fits were obtained for each BPNR width in Figure 3, and peak values were correlated to BPNR thicknesses using a linear monoelemental HAADF intensity-thickness relation $I \propto t$, where I is the intensity cross-section peak value and t is the corresponding ribbon thickness,[40] as shown in Figure S11 for both types of BPNRs. From an initial t = 17 nm, the zigzag (armchair) BPNR was reduced to a minimum of t = 4.4 nm (8.1 nm) before breaking into a

nanogap. This observation opens up a great opportunity for manipulating BP's thickness by calibrating the dose of the electron exposure for a given BP stack thickness and width.

CONCLUSION

We have demonstrated the fabrication of 1D nanostructures in suspended few-layer BPNRs. Using TEM, we nanosculpted nanometer-scale pores and showed their elliptical expansion under electron irradiation due to edge-dependent energy barriers for atomic removal. We have also demonstrated sub-10 nm wide zigzag and armchair BPNRs in the few-layer regime. Finally, using STEM-based nanosculpting and imaging, we showed that BPNRs can be narrowed and thinned with sub-nanometer precision. One drawback of nanosculpting is its low-throughput, limiting high-volume production. However, it provides atomic resolution and sub-nanometer-precise fabrication possibilities and is suitable for making nanostructures for fundamental studies and *in situ* characterization. We speculate that the BPNR length can be, in principle, extended similar to larger-scale TEM cutting of metals and graphene,[41] and future work could address the stability of long aspect ratio nanoribbons. In the future, tailoring BPNR shapes would allow the creation of local junctions with controlled width and thickness to achieve modulated band gap regions. STEM-based nanosculpting may also be useful for fabrication of multi-terminal devices with nanometer-scale features.

METHODS

Few-Layer BP Exfoliation

Square arrays of 300–400 nm diameter holes spaced 10 μm apart were patterned in silicon nitride (SiN_x) membranes with a focused ion beam.[34] Few-layer BP dispersions were produced by mechanically exfoliating BP onto a SiO_2 substrate followed by sonication (Branson 2510, 40 kHz, 80 W) in DMF for 1 h at room temperature. The BP–DMF dispersions were drop-cast onto holey carbon TEM grids or SiN_x membranes and then dried in 100% Ar for 12 h at room temperature. To eliminate liquid traces and minimize hydrocarbon contamination, samples were then annealed at 250 °C in 10% H_2/90% Ar for 1 h. Holey SiN_x samples were used for AFM measurements, while carbon grid samples were used in (S)TEM. Atmospheric exposure was limited to 5–10 min before AFM and (S)TEM measurements.

Atomic Force Microscopy

Suspended few-layer BP flakes were identified on holey SiN_x membranes using optical microscopy. AFM measurements were carried out in tapping mode using a Bruker Dimension Icon AFM.

Transmission Electron Microscopy

High-resolution TEM images were taken with a JEOL 2010F TEM operating at 200 kV. Nanopores were drilled by fully focusing (*i.e.*, condensing) an electron beam, with probe current and size of 8.0 nA and 1 nm, respectively, for ~1–2 s. Nanoconstrictions and nanogaps were formed by exposing the as-formed nanopores to a broad TEM beam (electron irradiation), corresponding to a current density of around 6.1×10^{-2} pA/nm^2. The

instrument's phosphor screen was used to measure the current density. A resolution limit of 0.11 nm is attributed to the microscope (Figure S6.2).

Scanning Transmission Electron Microscopy

High-angle annular dark-field STEM images were taken with a CEOS aberration-corrected JEOL ARM 200CF TEM. Unless otherwise noted, all HAADF STEM images were taken at 200 kV. Thickness measurements of few-layer BP flakes suspended on holey carbon films using the electron cross-section formula can be found in section S1. Nanopores were first drilled in the spot mode for ~1–2 min with a probe current and size of ~300 pA and 0.15 nm, respectively. Pores were controllably sculpted into BPNRs and subsequently nanogaps by directing the beam along the nanopore edges in spot mode using a 0.1 nm probe with a 14 pA current. This probe was also used during STEM imaging (rastering). Intensity cross sections of HAADF STEM BPNR images were fitted with moving average profiles and a 0.10 sampling proportion. BPNR thicknesses determined with these cross sections include an error of ±0.2 nm. Samples were tilted to the [001] zone axis prior to sculpting and imaging. A resolution limit of 0.08 nm is attributed to the microscope (Figure S6.2).

Selected Area Electron Diffraction

SAED images were taken in a JEOL 2010F operating at 200 kV. A selected area aperture with an effective diameter of 1 μm was used. SAED patterns were used to tilt samples to the [001] zone axis prior to sculpting and imaging.

Theoretical Methods

The Vienna *Ab Initio* Simulation Package (VASP) was used for plane-wave DFT calculations.[42] The optB86b functional was used to include local effects and nonlocal effects, including the van der Waals interaction.[43–45] We used the projector-augmented wave (PAW) pseudopotentials and an energy cutoff of 500 eV.[46] For bulk BP, the atoms and cell were relaxed to critical forces of 0.001 eV/Å using a Monkhorst–Pack k-point sampling[47] of 9 × 12 × 4, which resulted in the optimized lattice constants of a = 4.35 Å (armchair), b = 3.33 Å (zigzag), and c = 10.51 Å. To form monolayer phosphorene, four atoms were removed from the bulk unit cell and a vacuum layer of 20 Å was used to prevent interaction between periodic images. The atoms were relaxed to cutoff forces of 0.001 eV/Å using a k-point sampling of 9 × 12 × 1.

Nanoribbons were formed by using the lattice vectors and atomic coordinates from the phosphorene sheet. For armchair and both zigzag terminations, the unit cell contained one primitive unit cell parallel to the edge, and for both 2 × 1 supercell reconstructions of the ZZ-2 edge, the unit cell contained two primitive unit cells parallel to the edge. For all cases, the unit cell contained eight primitive unit cells perpendicular to the edge. An in-plane vacuum of about 20 Å was formed to minimize interaction between periodic images of the nanoribbons. These nanoribbon coordinates were relaxed to a force cutoff of 0.01 eV/Å using k-point samplings of 1 × 9 × 1 for armchair, 1 × 12 × 1 for both zigzag terminations, and 1 × 6 × 1 for both ZZ-2 reconstructions.

We computed the energy barriers for removing single atoms from the phosphorene edges by using the NEB method[48] in the VTST version of VASP with an improved tangent estimate.[49] Sixteen intermediate steps (images) were formed using linear interpolation, with smaller shifts in the low separation region, where any potential energy barriers were expected to form. The already existing ribbons were extended perpendicular to the atom removal direction by three unit cells for armchair and both terminations of zigzag and by one unit cell for the ZZRC edges. This ensures negligible interaction between periodic images of the atom being removed. The removed atom is one which is closest to the edge (Figures 2a and S5) and is shifted up to about 10 Å from the edge to ensure converged energies. The end point geometries were converged to a force cutoff of 0.01 eV/Å with k-point samplings of 1 × 3 × 1 for all cases. Atoms on the edge opposite where the atom was removed were held fixed to speed up convergence, and the NEB algorithm was converged to a force cutoff of 0.05 eV/Å.

To form the nanoribbons used in calculating band structures, the geometries were converged to force cutoffs of 0.01 eV/Å, and the number of k-points was chosen such that the product of the lattice vector and number of k-points was at least as large as the same value for the bulk. An in-plane vacuum of about 10 Å was used to prevent interaction between periodic images. At least five bands were used per atom to ensure well-converged bands, and 200 k-points were used along the high symmetry directions, found using the AFLOW tool.[50] To calculate the charge densities for the edge, band structures were recomputed with 25 k-points along the high symmetry directions. Since the Kohn–Sham energy eigenvalues are output in ascending order for each k-point, the band numbering changes if bands cross. To circumvent this, regions in the band structures were identified where only the suspected edge bands crossed over each other and the corresponding k-points in these regions were included in the partial charge density calculations.

Supplementary Material

Refer to Web version on PubMed Central for supplementary material.

Acknowledgments

This work was supported in part by NIH Grant R21HG007856 and by NSF Grant EFRI 2-DARE (EFRI-1542707). The authors gratefully acknowledge use of the TEM in the NSF-MRSEC electron microscopy facility and the use of the AFM in the Nanoscale Characterization Facility, both at the University of Pennsylvania, and use of the STEM in the Center for Advanced Materials and Nanotechnology at Lehigh University. We thank Dr. D. Yates and Dr. M. Brukman at the University of Pennsylvania and Dr. R. Keyse at Lehigh University for their assistance. Calculations were performed using resources at the Center for Computational Innovations (CCI) at Rensselaer Polytechnic Institute. L.L. was supported by the Eugene P. Wigner Fellowship at Oak Ridge National Laboratory and also acknowledges work at the Center for Nanophase Materials Sciences, a DOE Office of Science User Facility. Work by X.L., S.H., and M.S.D., developing procedures for preparation of black phosphorus samples, was supported as part of the Solid-State Solar Thermal Energy Conversion Center, an Energy Frontier Research Center funded by the U.S. DOE, Office of Science, Basic Energy Sciences, under Award #DE SC0001299.

References

1. Liu H, Neal AT, Zhu Z, Luo Z, Xu X, Tománek D, Ye PD. Phosphorene: An Unexplored 2D Semiconductor with a High Hole Mobility. ACS Nano. 2014; 8:4033–4041. [PubMed: 24655084]
2. Xia F, Wang H, Jia Y. Rediscovering Black Phosphorus as an Anisotropic Layered Material for Optoelectronics and Electronics. Nat Commun. 2014; 5:4458. [PubMed: 25041752]

3. Ling X, Wang H, Huang S, Xia F, Dresselhaus MS. The Renaissance of Black Phosphorus. Proc Natl Acad Sci USA. 2015; 112:4523–4530. [PubMed: 25820173]
4. Castellanos-Gomez A, Vicarelli L, Prada E, Island JO, Narasimha-Acharya KL, Blanter SI, Groenendijk DJ, Buscema M, Steele GA, Alvarez JV, Zandbergen HW, Palacios JJ, van der Zant HSJ. Isolation and Characterization of Few-Layer Black Phosphorus. 2D Mater. 2014; 1:025001.
5. Hanlon D, Backes C, Doherty E, Cucinotta CS, Berner NC, Boland C, Lee K, Harvey A, Lynch P, Gholamvand Z, Zhang S, Wang K, Moynihan G, Pokle A, Ramasse QM, McEvoy N, Blau WJ, Wang J, Abellan G, Hauke F, et al. Liquid Exfoliation of Solvent-Stabilized Few-Layer Black Phosphorus for Applications Beyond Electronics. Nat Commun. 2015; 6:8563. [PubMed: 26469634]
6. Das S, Zhang W, Demarteau M, Hoffmann A, Dubey M, Roelofs A. Tunable Transport Gap in Phosphorene. Nano Lett. 2014; 14:5733–5739. [PubMed: 25111042]
7. Tran V, Soklaski R, Liang Y, Yang L. Layer-Controlled Band Gap and Anisotropic Excitons in Few-Layer Black Phosphorus. Phys Rev B: Condens Matter Mater Phys. 2014; 89:235319.
8. Li L, Yu Y, Ye GJ, Ge Q, Ou X, Wu H, Feng D, Chen XH, Zhang Y. Black Phosphorus Field-Effect Transistors. Nat Nanotechnol. 2014; 9:372–377. [PubMed: 24584274]
9. Qiao J, Kong X, Hu Z-X, Yang F, Ji W. High-Mobility Transport Anisotropy and Linear Dichroism in Few-Layer Black Phosphorus. Nat Commun. 2014; 5:4475. [PubMed: 25042376]
10. Yuan H, Liu X, Afshinmanesh F, Li W, Xu G, Sun J, Lian B, Curto AG, Ye G, Hikita Y, Shen Z, Zhang SC, Chen X, Brongersma M, Hwang HY, Cui Y. Polarization-Sensitive Broadband Photodetector Using a Black Phosphorus Vertical P-N Junction. Nat Nanotechnol. 2015; 10:707–713. [PubMed: 26030655]
11. Wood JD, Wells SA, Jariwala D, Chen KS, Cho E, Sangwan VK, Liu X, Lauhon LJ, Marks TJ, Hersam MC. Effective Passivation of Exfoliated Black Phosphorus Transistors Against Ambient Degradation. Nano Lett. 2014; 14:6964–6970. [PubMed: 25380142]
12. Avsar A, Vera-Marun IJ, Tan JY, Watanabe K, Taniguchi T, Castro Neto AH, Ozyilmaz B. Air Stable Transport in Graphene Contacted, Fully Encapsulated Ultra Thin Black Phosphorus-Based Field-Effect Transistors. ACS Nano. 2015; 9:4138–4145. [PubMed: 25769342]
13. Li X, Wang X, Zhang L, Lee S, Dai H. Chemically Derived, Ultrasmooth Graphene Nanoribbon Semiconductors. Science. 2008; 319:1229–1232. [PubMed: 18218865]
14. Son YW, Cohen ML, Louie SG. Energy Gaps in Graphene Nanoribbons. Phys Rev Lett. 2006; 97:216803. [PubMed: 17155765]
15. Guo H, Lu N, Dai J, Wu X, Zeng XC. Phosphorene Nanoribbons, Phosphorus Nanotubes, and Van der Waals Multilayers. J Phys Chem C. 2014; 118:14051–14059.
16. Xu LC, Song XJ, Yang Z, Cao L, Liu RP, Li XY. Phosphorene Nanoribbons: Passivation Effect on Bandgap and Effective Mass. Appl Surf Sci. 2015; 324:640–644.
17. Qi ZJ, Rodríguez-Manzo JA, Botello-Méndez AR, Hong SJ, Stach EA, Park YW, Charlier JC, Drndić M, Johnson ATC. Correlating Atomic Structure and Transport in Suspended Graphene Nanoribbons. Nano Lett. 2014; 14:4238–4244. [PubMed: 24954396]
18. Song B, Schneider GF, Xu Q, Pandraud G, Dekker C, Zandbergen H. Atomic-Scale Electron-Beam Sculpting of Near-Defect-Free Graphene Nanostructures. Nano Lett. 2011; 11:2247–2250. [PubMed: 21604710]
19. Tapasztó L, Dobrik G, Lambin P, Biró LP. Tailoring the Atomic Structure of Graphene Nanoribbons by Scanning Tunnelling Microscope Lithography. Nat Nanotechnol. 2008; 3:397–401. [PubMed: 18654562]
20. Fischbein MD, Drndić M. Electron Beam Nanosculpting of Suspended Graphene Sheets. Appl Phys Lett. 2008; 93:113107.
21. Liu K, Feng J, Kis A, Radenovic A. Atomically Thin Molybdenum Disulfide Nanopores with High Sensitivity for DNA Translocation. ACS Nano. 2014; 8:2504–2511. [PubMed: 24547924]
22. Lee S, Yang F, Suh J, Yang S, Lee Y, Li G, Sung Choe H, Suslu A, Chen Y, Ko C, Park J, Liu K, Li J, Hippalgaonkar K, Urban JJ, Tongay S, Wu J. Anisotropic In-Plane Thermal Conductivity of Black Phosphorus Nanoribbons at Temperatures Higher than 100 K. Nat Commun. 2015; 6:8573. [PubMed: 26472285]

23. Chaves A, Low T, Avouris P, Cakir D, Peeters FM. Anisotropic Exciton Stark Shift in Black Phosphorus. Phys Rev B: Condens Matter Mater Phys. 2015; 91:155311.
24. Kang J, Wood JD, Wells SA, Lee JH, Liu X, Chen KS, Hersam MC. Solvent Exfoliation of Electronic-Grade, Two-Dimensional Black Phosphorus. ACS Nano. 2015; 9:3596–3604. [PubMed: 25785299]
25. Favron A, Gaufrès E, Fossard F, Phaneuf-L'Heureux A-L, Tang NY-W, Lévesque PL, Loiseau A, Leonelli R, Francoeur S, Martel R. Photooxidation and Quantum Confinement Effects in Exfoliated Black Phosphorus. Nat Mater. 2015; 14:826–832. [PubMed: 26006004]
26. Tao J, Shen W, Wu S, Liu L, Feng Z, Wang C, Hu C, Yao P, Zhang H, Pang W, Duan X, Liu J, Zhou C, Zhang D. Mechanical and Electrical Anisotropy of Few-Layer Black Phosphorus. ACS Nano. 2015; 9:11362–11370. [PubMed: 26422521]
27. Luo Z, Maassen J, Deng Y, Du Y, Lundstrom MS, Ye PD, Xu X. Anisotropic In-Plane Thermal Conductivity Observed in Few-Layer Black Phosphorus. Nat Commun. 2015; 6:8572. [PubMed: 26472191]
28. Wu RJ, Topsakal M, Low T, Robbins MC, Haratipour N, Jeong JS, Wentzcovitch RM, Koester SJ, Mkhoyan KA. Atomic and Electronic Structure of Exfoliated Black Phosphorus. J Vac Sci Technol, A. 2015; 33:060604.
29. Rosenstein JK, Wanunu M, Merchant CA, Drndić M, Shepard KL. Integrated Nanopore Sensing Platform with Sub-Microsecond Temporal Resolution. Nat Methods. 2012; 9:487–492. [PubMed: 22426489]
30. Liu X, Wood JD, Chen KS, Cho E, Hersam MC. *In Situ* Thermal Decomposition of Exfoliated Two-Dimensional Black Phosphorus. J Phys Chem Lett. 2015; 6:773–778. [PubMed: 26262651]
31. Fortin-Deschênes M, Levesque PL, Martel R, Moutanabbir O. Dynamics and Mechanisms of Exfoliated Black Phosphorus Sublimation. J Phys Chem Lett. 2016; 7:1667–1674. [PubMed: 27097073]
32. Ramasubramaniam A, Muniz AR. *Ab Initio* Studies of Thermodynamic and Electronic Properties of Phosphorene Nanoribbons. Phys Rev B: Condens Matter Mater Phys. 2014; 90:085424.
33. Wang G, Loh GC, Pandey R, Karna SP. Out-of-Plane Structural Flexibility of Phosphorene. Nanotechnology. 2016; 27:055701. [PubMed: 26671643]
34. Puster M, Rodríguez-Manzo JA, Balan A, Drndić M. Toward Sensitive Graphene Nanoribbon-Nanopore Devices by Preventing Electron Beam-Induced Damage. ACS Nano. 2013; 7:11283–11289. [PubMed: 24224888]
35. Puster M, Balan A, Rodríguez-Manzo JA, Danda G, Ahn JH, Parkin W, Drndić M. Cross-Talk Between Ionic and Nanoribbon Current Signals in Graphene Nanoribbon-Nanopore Sensors for Single-Molecule Detection. Small. 2015; 11:6309–6316. [PubMed: 26500023]
36. Guan J, Zhu Z, Tománek D. Phase Coexistence and Metal-Insulator Transition in Few-Layer Phosphorene: A Computational Study. Phys Rev Lett. 2014; 113:046804. [PubMed: 25105644]
37. Wu M, Fu H, Zhou L, Yao K, Zeng XC. Nine New Phosphorene Polymorphs with Non-Honeycomb Structures: A Much Extended Family. Nano Lett. 2015; 15:3557–3562. [PubMed: 25844524]
38. Vierimaa V, Krasheninnikov A, Komsa HP. Phosphorene Under Electron Beam: From Monolayer to One-Dimensional Chains. Nanoscale. 2016; 8:7949–7957. [PubMed: 27004746]
39. Mehboudi M, Dorio AM, Zhu W, van der Zande A, Churchill HOH, Pacheco-Sanjuan AA, Harriss EO, Kumar P, Barraza-Lopez S. Two-Dimensional Disorder in Black Phosphorus and Monochalcogenide Monolayers. Nano Lett. 2016; 16:1704–1712. [PubMed: 26866878]
40. Erni R, Heinrich H, Kostorz G. Quantitative Characterisation of Chemical Inhomogeneities in Al-Ag Using High-Resolution Z-Contrast STEM. Ultramicroscopy. 2003; 94:125–133. [PubMed: 12505761]
41. Lu Y, Merchant CA, Drndić M, Johnson ATC. *In Situ* Electronic Characterization of Graphene Nanoconstrictions Fabricated in a Transmission Electron Microscope. Nano Lett. 2011; 11:5184–5188. [PubMed: 22026483]
42. Kresse G, Furthmüller J. Efficient Iterative Schemes for *Ab Initio* Total-Energy Calculations Using a Plane-Wave Basis Set. Phys Rev B: Condens Matter Mater Phys. 1996; 54:11169.

43. Dion M, Rydberg H, Schröder E, Langreth DC, Lundqvist BI. Van der Waals Density Functional for General Geometries. Phys Rev Lett. 2004; 92:246401. [PubMed: 15245113]
44. Román-Pérez G, Soler JM. Efficient Implementation of a Van der Waals Density Functional: Application to Double-Wall Carbon Nanotubes. Phys Rev Lett. 2009; 103:096102. [PubMed: 19792809]
45. Klimeš J, Bowler DR, Michaelides A. Van der Waals Density Functionals Applied to Solids. Phys Rev B: Condens Matter Mater Phys. 2011; 83:195131.
46. Blöchl PE. Projector Augmented-Wave Method. Phys Rev B: Condens Matter Mater Phys. 1994; 50:17953.
47. Monkhorst H, Pack J. Special Points for Brillouin Zone Integrations. Phys Rev B. 1976; 13:5188–5192.
48. Jónsson H, Mills G, Jacobsen KW. Nudged Elastic Band Method for Finding Minimum Energy Paths of Transitions. Classical and Quantum Dynamics in Condensed Phase Simulations. 1997; 1:385–404.
49. Henkelman G, Jónsson H. Improved Tangent Estimate in the Nudged Elastic Band Method for Finding Minimum Energy Paths and Saddle Points. J Chem Phys. 2000; 113:9978–9985.
50. Setyawan W, Curtarolo S. High-Throughput Electronic Band Structure Calculations: Challenges and Tools. Comput Mater Sci. 2010; 49:299–312.
51. Liang L, Wang J, Lin W, Sumpter BG, Meunier V, Pan M. Electronic Bandgap and Edge Reconstruction in Phosphorene Materials. Nano Lett. 2014; 14:6400–6406. [PubMed: 25343376]

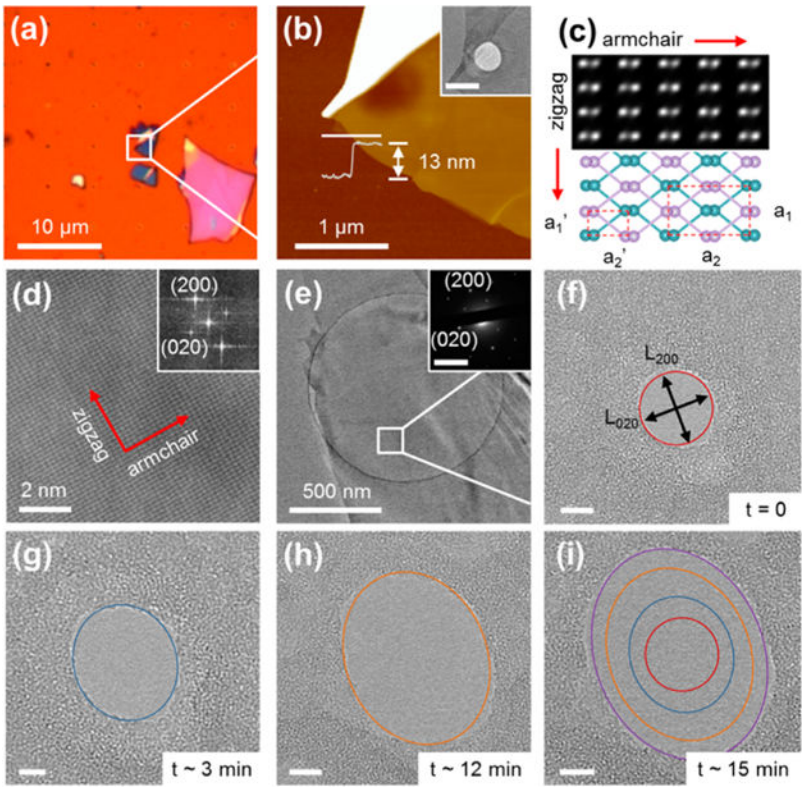

Figure 1.

Characterization of few-layer BP flakes and the elliptical expansion of nanopores. (a) Optical micrograph of a holey SiN_x membrane used to perform AFM measurements after few-layer BP deposition. (b) AFM image of a suspended few-layer sample indicated by the white square in (a) and an AFM line scan across the SiN_x/BP interface indicating a 13 nm thick flake. The inset is a HRTEM image of the flake. Inset scale bar is 1 μm. The white region in (b) corresponds to a thick, folded region of the BP flake and appears more opaque in the TEM, as expected. (c) STEM simulation (top) and illustration (bottom) of AB-stacked bilayer BP with zigzag and armchair lattice constants a_1 and a_2, respectively, in addition to half-lattice constants a_1' and a_2'. A and B layers are highlighted in different colors. (d) HAADF STEM image of the few-layer BP lattice indicating spacings that are consistent with a_1' (200) and a_2' (020) (the inset is the corresponding fast Fourier transform). (e) HRTEM image and corresponding selected area electron diffraction pattern (inset) of a few-layer BP flake suspended on a holey carbon grid. (f) HRTEM image of the region indicated by the white square in (e), containing a 10 nm diameter nanopore with dimensions of L_{200} and L_{020} in the zigzag and armchair directions, respectively. Over a period of 15 min of electron irradiation (current density = 6.1×10^{-2} pA/nm^2), the pore expanded elliptically with eccentricity evolving from (f) $L_{200}/L_{020} = 1.0$ to (g) 1.2, (h) 1.3, and (i) 1.4. All scale bars in (f–i) are 5 nm.

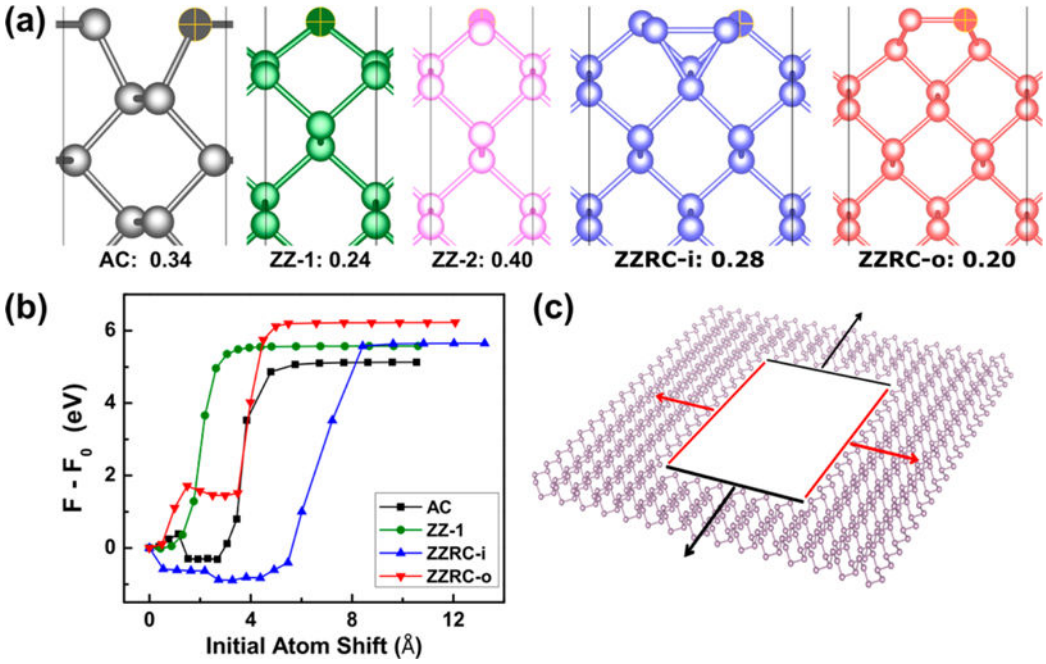

Figure 2.

Structure and energetics of the phosphorene edges as computed using density functional theory. (a) Overhead views of the armchair (AC), zigzag single termination (ZZ-1), zigzag double termination (ZZ-2), inner-shifted reconstruction of the ZZ-2 edge (ZZRC-i),[51] and outer-shifted reconstruction of the ZZ-2 edge (ZZRC-o)[32] phosphorene edges. The corresponding edge energies for the supercells used are given in eV/Å to quantify the thermodynamic stability. (b) Energy landscapes for removing a single atom from phosphorene edges *via* the NEB method. (c) Schematic illustrating the observation of an elliptical nanopore in phosphorene. The armchair edges (black) recede faster than the most stable zigzag edge (ZZRC-o) due to the greater energy barrier for removing atoms from the latter edge, which results in relatively longer nanopore dimensions in the zigzag (200) direction (Figure 1f–i).

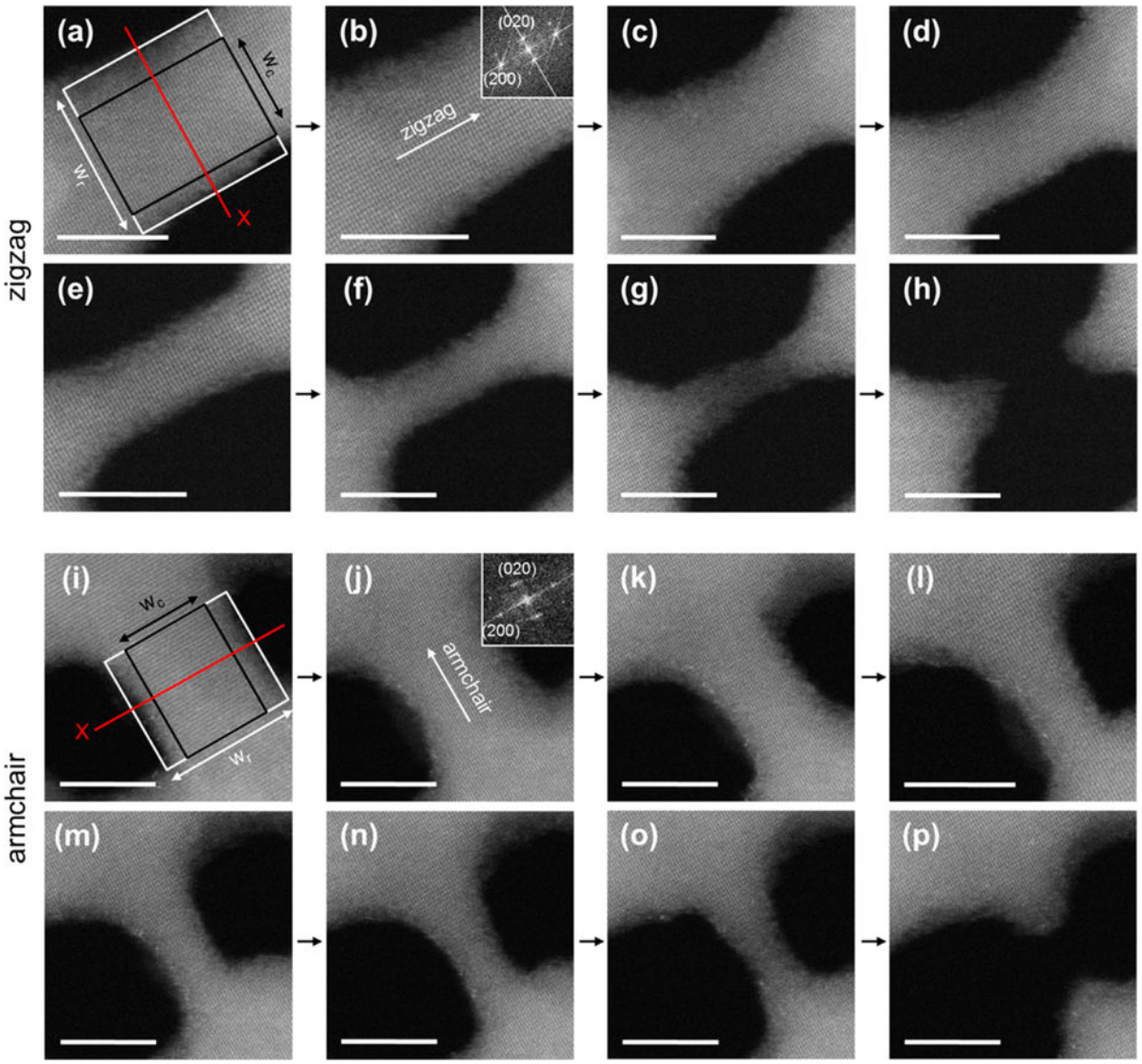

Figure 3.

STEM nanosculpting of zigzag and armchair few-layer BPNRs. HAADF STEM images of an (a–h) 8.0 nm long zigzag and (i–p) 6.5 nm long armchair nanoribbon. (a,i) w_r and w_c are the total and crystalline BPNR widths, respectively (see also Figure S6.1). Thinning of the ribbons from (a) to (h) and from (i) to (p) was observed by using the HAADF intensity-thickness correlation for each panel along the red line X (indicated in (a) and (i); see also Figure S11). The fast Fourier transforms in the insets of (b) and (j) indicate lattice spacings of 1.65 and 2.28 Å, consistent with a_1' and a_2', respectively. For the zigzag case, w_r is initially (a) 7.2 nm and subsequently narrowed to (b) 6.0, (c) 5.7, (d) 4.6, (e) 2.8, (f) 2.2, and (g) 1.7 nm. The corresponding w_c values are (a) 5.6, (b) 4.6, (c) 4.3, (d) 3.1, (e) 1.9, (f) 1.0, and (g) 0 nm. For the armchair case, the values for w_r are (i) 6.3, (j) 5.8, (k) 4.2, (l) 3.1, (m) 2.8, (n) 2.5, and (o) 2.1 nm. The corresponding w_c values are (i) 4.9, (j) 4.2, (k) 3.0, (l) 1.4, (m) 0.9, (n) 0.5, and (o) 0 nm. After the BPNRs break, (h) 3.5 and (p) 2.8 nm wide nanogaps remain. All scale bars in (a–p) are 5 nm.

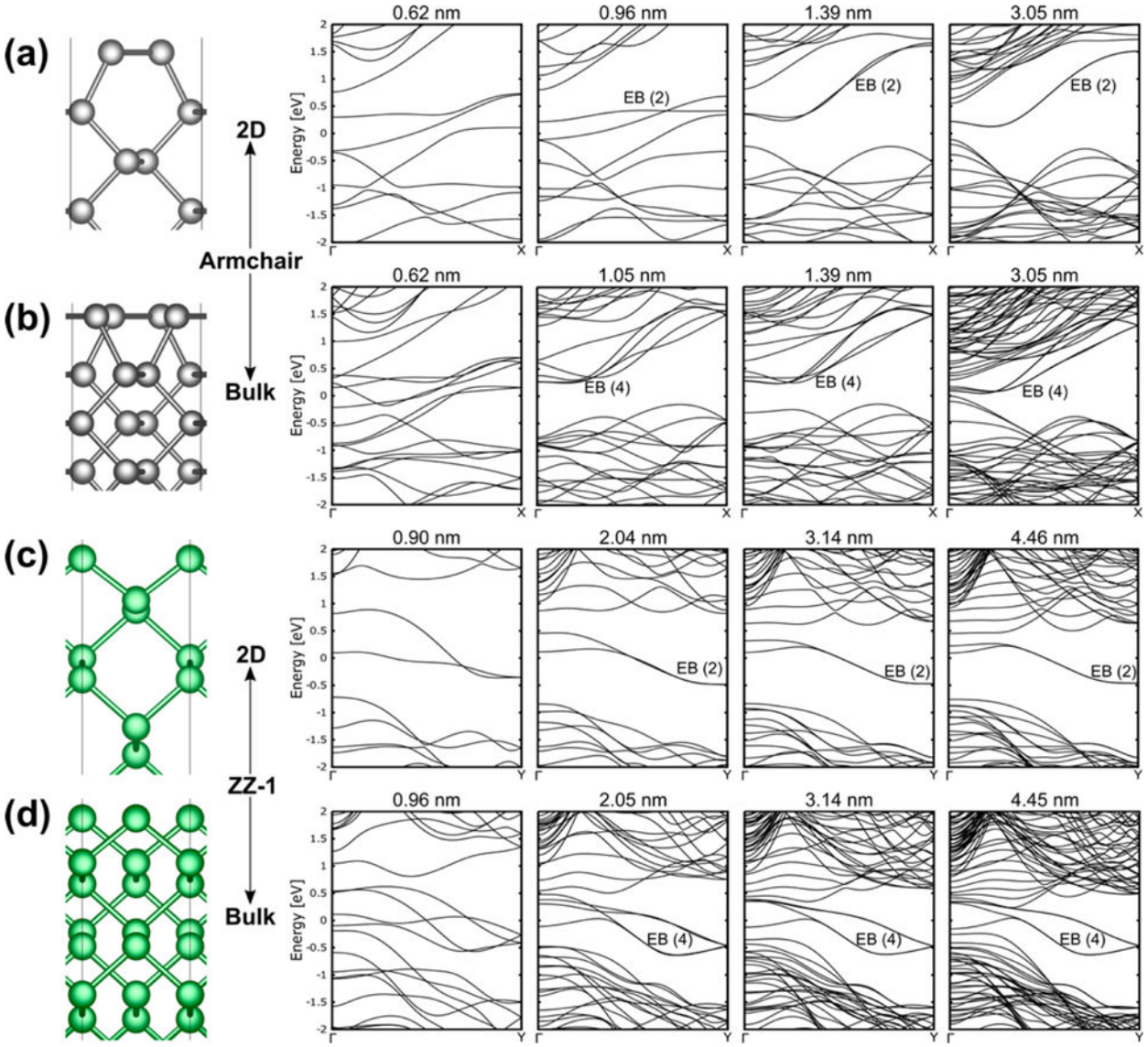

Figure 4.

DFT-calculated electronic band structures of BPNRs based on the experimentally realized crystalline widths. The edge bands are indicated by EB with the number of such bands in parentheses. The Fermi level has been set to 0 eV. The schematic diagrams on the left indicate the corresponding BPNR structure: (a) single-layer armchair; (b) bulk armchair; (c) single-layer ZZ-1; (d) bulk ZZ-1.